Settling of localized particle plumes in a quiescent water tank

Till Zürner, Clément Toupoint, David de Souza, Dylan Mezouane, Romain Monchaux

Settling of localized particle plumes in a quiescent water tank

Till Zürner, Clément Toupoint, David De Souza, Dylan Mezouane, and Romain Monchaux*
UME, ENSTA Paris, Institut Polytechnique de Paris, 828 Boulevard des Maréchaux, 91120 Palaiseau, France
(Dated: December 14, 2022)

The fall or rise of inertial particles plumes in an initially quiescent fluid is ubiquitous in natural and industrial processes. Disentangling the influence of the numerous parameters of these systems on the plume velocity is thus a major issue. Moreover, understanding the energy transfer between the two phases and the structure of induced flow is another very relevant question. A specific experiment has been designed to tackle these problems. A continuous plume of inertial particles released above the center of a still water tank generates a large-scale recirculation flow. The present experimental study investigates the stationary settling dynamics and induced flow properties using various particle populations with particle-to-fluid density ratios from 3.8 to 14.3, Archimedes numbers 4 to 580 and mass fractions 10^{-6} to 10^{-3}, revealing an unexplored region of the parameter space. The fluid and particle velocities are measured simultaneously by two cameras, utilizing optical filtering and image post-processing. It is found that the settling in the laboratory frame generally follows the terminal velocity predicted using the Schiller-Naumann drag. The particle velocity relative to the surrounding fluid is unaffected by the particle mass fraction and always hindered due to the kinetic energy transferred to the fluid. This transfer of energy is most effective for low Archimedes numbers. All modifications of the settling behavior due to the particle mass fraction are caused by the back-reaction of the induced flow on the particles, no direct particle-particle interactions are observed.

I. INTRODUCTION

The dynamics of particles settling in a fluid are a complex topic that still poses many open questions. They are relevant in both natural and industrial phenomena such as cloud formation in the atmosphere [1], volcanic ash propagation [2], transmission of pathogens [3], surface coating [4] or mineral ore processing [5]. Particles can either be released in an externally forced flow or in a fluid at rest. In the former case, if the imposed flow is turbulent, the most relevant questions are linked to the preferential sampling of the turbulent structures by the inertial particles, their tendency to clustering, their settling velocity alteration, the impact all these phenomena have on their probability to collide [6–8] and finally the impact the particles have on the carrier turbulence properties, the so-called two-way coupling [9]. The parameter space is at least of dimension five to take into account particle inertia, density disparity, turbulence, gravity and loading. Without the presence of an external turbulent fluid flow, the behavior of inertial particles in initially quiescent fluids can be an equally complicated problem [10]. Their behavior depends on the particle and fluid properties, the loading and the duration of the seeding [11]. The particle dynamics may evolve inside a fluid that globally remains at rest or they can induce a flow in the fluid (which can even turn turbulent). In the latter case, the particles will interact with the flow they themselves created. This could be considered as the most elementary two-way coupling situation.

Most of the aforementioned studies consider particle populations that are evenly distributed within the whole carrier fluid. A spatially varying particle concentration introduces an additional layer of complexity and is studied less often. Indeed, the way particle are released in space and in time with respect to the fluid container geometry, will lead to very different flow conditions as detailed in the subsequent references in this paragraph. The most common configuration for localized distributions are clouds of particles of finite length in all three spatial dimensions. They are dominated by highly transient interactions between the particles and the fluid, especially at the interface between cloud and vacant fluid. Vortex rings at the cloud front entrain the surrounding fluid and deform the shape of the cloud [12–14]. These systems are of interest as the dependence of their behavior on the particle properties can be used to, for instance, determine the particle size distribution [13, 15]. Continuously falling configurations (i.e., distributions restricted in the horizontal plane only) include thin curtains [16] and more voluminous particle plumes [11, 17]. Particle curtains are of interest, for instance, in solar power generation [18] while plumes are relevant in material transport, sedimentation phenomena as well as health and safety considerations [17, 19, 20].

In the present study, the focus lies on particle plumes as a system of localized ensembles of continuously settling particles and their influence on the carrier fluid. Specifically, the stationary settling behavior of the particle plume is investigated and compared to theoretical predictions for a single particle. Simultaneously, the fluid flow induced by the plume is measured and the corresponding energy transfer is characterized. The recorded data also allow the evaluation of the particle motion relative to the local fluid velocity. The choice of water as carrier fluid implies that, as opposed to highly viscous oils, the flow initiated by the falling particle is at higher Reynolds numbers than in creeping flow situations [21], transitioning towards non-linear flow dynamics. Another consequence is that the particle-to-fluid density ratio will be of order 1 to 10 regardless of the chosen material

* Corresponding author: romain.monchaux@ensta-paris.fr

for the settling particles. This is very distinctive from studies carried out in air where density ratios are generally of the order 1000. Our intention is to cover density ratios up to almost 15 which is quite unusual; most studies in water are considering glass or sand whose densities are around twice that of water. The particles we have selected are rather small (between 32 µm and 200 µm) compared to many studies in the literature. Finally, the loadings we are considering (volume fractions below 1 %) are also small compared to those more commonly found in the literature. As a result, we are mapping a rather unexplored region of the parameter space that is filling a gap between existing studies.

We first present the theoretical and empirical framework of our study in section II, introducing our notations and reference cases. We then provide details about the experimental setup (section III), a water tank in which falling particle plumes generate a large scale recirculating flow, and we describe the multiphase measurement system we have designed to simultaneously record particles and fluid velocities. Section IV gathers all our results about particle dynamics, fluid statistics, energy transfers and particle concentration. Discussions and conclusions are given in the last section V.

II. THEORY AND EMPIRICAL RELATIONS

The simplest canonical system describing particle settling consists of a single solid sphere of diameter d_p and mass density ρ_p moving with a velocity $\boldsymbol{v}$ in a fluid with mass density ρ_f, kinematic viscosity ν and quiescent velocity field $\boldsymbol{u} = \boldsymbol{0}$. The particle motion is driven by the vertical buoyancy force $V_\mathrm{p}(\rho_\mathrm{f} - \rho_\mathrm{p})g$ with the particle volume $V_\mathrm{p} = \pi d_\mathrm{p}^3/6$ and the acceleration due to gravity $g = 9.81\,\mathrm{m/s^2}$. The density ratio $\Gamma = \rho_\mathrm{p}/\rho_\mathrm{f}$ determines whether the particle is rising ($\Gamma < 1$), sinking ($\Gamma > 1$) or remains motionless ($\Gamma = 1$) in the still fluid. Opposing the buoyancy is the drag force of the fluid $C_\mathrm{D}\rho_\mathrm{f}|\Delta\boldsymbol{v}|^2\pi d_\mathrm{p}^2/8$ which acts in the opposite direction of the slip velocity $\Delta\boldsymbol{v} = \boldsymbol{v} - \boldsymbol{u}|_\mathrm{p}$ where $\boldsymbol{u}|_\mathrm{p}$ is the fluid velocity at the particle position, i.e., $\Delta\boldsymbol{v}$ is the particle motion relative to the surrounding fluid. The drag coefficient C_D is a complicated function of $|\Delta\boldsymbol{v}|$ and given in terms of the particle Reynolds number $\mathrm{Re_p} = |\Delta\boldsymbol{v}|d_\mathrm{p}/\nu$. Due to its simplicity, many studies utilize the Stokes drag $C_\mathrm{D} = 24/\mathrm{Re_p}$ which is valid for slow moving particles with $\mathrm{Re_p} < 1$. However, in recent years it has become more commonplace to consider drag coefficients in the form $C_\mathrm{D} = (24/\mathrm{Re_p})f_\mathrm{D}(\mathrm{Re_p})$, more accurate for $\mathrm{Re_p} > 1$, to model particle movement employing empirical drag models f_D. In the present study, the Stokes drag is compared with the Schiller-Naumann (SN) drag $f_\mathrm{D} = f_\mathrm{SN} = 1 + 0.150\,\mathrm{Re_p^{0.687}}$ valid for $\mathrm{Re_p} < 800$ [22]. It accounts for an increase in drag due to the formation of recirculation zones and the eventual detachment of vortices in the wake of the particle.

Under the influence of buoyancy and drag, the particle slip velocity eventually reaches a constant value – the terminal velocity v_t. By balancing the two forces, we obtain the terminal Reynolds number $\mathrm{Re_t} = |v_\mathrm{t}|d_\mathrm{p}/\nu$ which is given by

$$\mathrm{Re_t} f_\mathrm{D}(\mathrm{Re_t}) = \frac{\mathrm{Ar}}{18}\,. \tag{1}$$

The Archimedes number $\mathrm{Ar} = |\Gamma - 1|gd_\mathrm{p}^3/\nu^2$ describes the particle properties as the ratio of buoyancy and viscous forces (an alternative quantity is the Galileo number $\mathrm{Ga} = \sqrt{\mathrm{Ar}}$). For the Stokes drag ($f_\mathrm{D} = f_\mathrm{St} = 1$), equation (1) reduces to $\mathrm{Re_{St}} = \mathrm{Ar}/18$ and the terminal velocity is $v_\mathrm{St} = -d_\mathrm{p}^2(\Gamma - 1)g/18$. To determine the terminal velocity v_SN and its corresponding terminal Reynolds number $\mathrm{Re_{SN}}$ for the Schiller-Naumann model f_SN, equation (1) has to be solved numerically. In this manuscript, the terminal velocity refers exclusively to the theoretical value stemming from the balance of drag and buoyancy. The corresponding experimental values in the laboratory frame of reference are denoted as settling velocity and include other effects like particle concentration and background fluid flow.

The theoretical treatment of an ensemble of many particles is difficult due to their complex interactions. Instead, it is common to derive empirical relations from experimental data. An often invoked formula for the dependence of the average settling velocity on the particle volume fraction Φ_V is the Richardson-Zaki (RZ) law [23]. It is formulated for a suspension of homogeneously distributed particles in a vertical pipe. The settling velocity v_z in the laboratory reference frame is commonly determined by measuring the time the particles take to fall a certain distance or by regulating an upwards flow in the pipe to a speed, at which the particles float at a constant height [24]. The Richardson-Zaki law predicts that the settling velocity v_z slows down with increasing volume fraction

$$v_z = \gamma v_\mathrm{t}(1 - \Phi_V)^n\,. \tag{2}$$

The exponent n is a function of the terminal Reynolds number $\mathrm{Re_t}$ and reported by Rowe [25] as $n(\mathrm{Re}_t) = 2.35\,(2 + 0.175\,\mathrm{Re_t^{3/4}})/(1 + 0.175\,\mathrm{Re_t^{3/4}})$. The original formula by Richardson and Zaki [23] was derived for high volume fractions $\Phi_V \geq 8\,\%$ and they extrapolated that v_z reaches the terminal velocity v_t for very low loadings $\Phi_V \ll 1$. However, further measurements revealed a hindering effect for dilute suspensions and an additional scaling factor $\gamma \approx 0.8$ to 0.9 was introduced [26].

The Richardson-Zaki law does not directly pertain to our experiment, since the configuration between a homogeneous particle distribution and a particle plume differs significantly. However, since this relation is often used to describe particle settling, comparing it to the present case and demonstrating the extend of its applicability is a worthwhile endeavor.

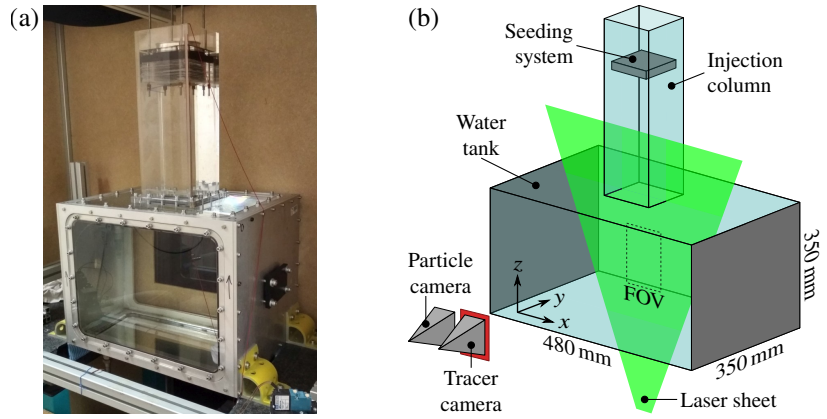

Figure 1: Experimental setup. (a) Photograph. (b) Illustration with labeled components and dimensions.

Material	Label	ρ_p (kg/m^3)	Γ
Ceramics	CER	3 800	3.8
Steel	STE	7 900	7.9
Inconel	INC	8 440	8.5
Tungsten carbide	TUN	14 300	14.3

Table I: Particle materials, their short label, mass density ρ_p and density ratio Γ at 20 °C. See also table II in the appendix for more details.

III. THE EXPERIMENTAL SET-UP

Figure 1 shows the experimental set-up. The water tank consists of an aluminium frame with PMMA windows and has the inner dimensions 480 mm × 350 mm × 350 mm. Centered on top of the tank sits an injection column with a cross-section of 130 mm × 130 mm and height 435 mm. It houses the particle seeding system which consists of a sieve and an electric actuator. The particles are evenly distributed onto the sieve and the actuator shakes the system to steadily release the particles into the experiment. The amplitude and frequency of the actuator as well as the amount of particles on top of the sieve are adjusted to give a variety of particle loadings. A stack of 16 horizontal grids with a mesh size of 2 mm is attached below the sieve to more evenly spread the particles over the cross-section of the seeding column [27].

The tank and the column are filled with water up to a height that fully covers the seeding system. At its average temperature of 20 °C (recorded with a RS 51 digital thermometer and a K-type thermocouple) the water has a density of $\rho_\mathrm{f} = 998\,\mathrm{kg/m^3}$ and a kinematic viscosity of $\nu = 10^{-6}\,\mathrm{m^2/s}$ [28].

A. Particles

The particles used in the present study are selected to cover a large area of the parameter space. Since this requires many populations of different sizes and materials, they cannot be specifically engineered to meet idealized experimental conditions and are used as they come. Among others this results in a low intensity of light scattered by the particles and a relatively large deviation from the ideal spherical geometry. These issues will be discussed in the following sections where they become relevant.

Four density ratios Γ between 3.8 and 14.3 are investigated using the materials ceramics (CER), steel (STE), inconel (INC) and tungsten carbide (TUN). Their properties are listed in table I. The polydisperse raw populations of each material are split into sub-populations with a more narrow size distribution by sieving. The raw population is placed on a stack of sieves with successively smaller mesh size. The stack is shaken by a vibratory sieve shaker (Retsch AS 200 digit cA) until the mass of particles caught on each sieve changes by less than 0.5 % of the starting mass over a 5 minute interval. The sieved populations are denoted by their material label, the size of the sieve they were caught in and the previous sieve size in micrometer. For instance, CER 125–106 refers to ceramic particles that passed through a 125 µm sieve but remained in the next smaller sieve of 106 µm size. The sieves range from 32 µm to 200 µm.

The size distributions for the sieved particle populations are determined with a Keyence KHX-600 microscope. A representative subset of at least 1000 particles per population are photographed and an ellipse is fitted to the outer contour of each particle on the microscope images, giving their major and minor diameter a and b, respectively. The shape of the particles is characterized

by their elongation ratio a/b. The canonical case of spherical particles would result in $a/b = 1$ while ellipsoidal particles have $a/b > 1$. For most of the investigated populations, 80 % of the particles have an elongation ratio less than $(a/b)_{80} \approx 1.36$ (table II in the appendix). Only the inconel particles show stronger deformations with an 80$^{\text{th}}$ percentile of $(a/b)_{80} \approx 1.5$ and the smallest ceramic particle population CER 075–090 exhibits $(a/b)_{80} \approx 1.62$. Nonetheless, at these elongation ratios and for the observed range of $\mathrm{Re_p}$, the influence of the particle shape on the drag is negligibly small [29]. Each particle is assigned an equivalent diameter $d_{\mathrm{eq}} = \sqrt{ab}$ that corresponds to the diameter of a circle with the same area as the ellipse circumscribed around the particle. The characteristic diameter d_{p} of a particle population is then determined as the median value of the corresponding equivalent diameter distribution. A detailed list of the populations employed in this study along with their properties are given in table II of the appendix. The Archimedes number of all populations covers two orders of magnitude $4 \leq \mathrm{Ar} \leq 664$.

B. Measurement procedure

A Nd:YAG laser (Nano L 135-15 PIV by Litron Lasers) below the tank produces a vertical laser sheet with a thickness of 2 mm and a wavelength of 532 nm. It illuminates the x-z-plane in the center of the tank (see figure 1(b)). To visualize the fluid velocity field, 20 µm melamine resin based polymer particles coated with fluorescent rhodamine B (by Dantec Dynamics) are mixed into the water. The fluorescent dye absorbs the laser light and emits light at a shifted wavelength above 570 nm. In the following, the term "particle" refers exclusively to the inertial particles described in section III A and "tracer" to the fluorescent fluid tracers.

The particles and tracers are recorded using two VC-Imager SX 4M cameras from LaVision (focal length $f = 50$ mm). Both cameras are pointed at the same field of view (FOV) in the tank center and their focal planes are adjusted using Scheimpflug adapters. The first camera is directly recording the laser light scattered by both particles and tracers. The second camera employs an optical filter that blocks out the laser light and only allows the fluorescent light of the tracers to be recorded. Thus, the first, unfiltered camera is denoted as "particle camera" and the second, filtered camera as "tracer camera".

Since both particles and tracers appear on the particle camera image, they have to be separated in order to obtain correct particle dynamics. Even the largest particles (diameter ~ 200 µm) are imaged with an apparent diameter of ~ 5 px which is not significantly different from the tracers which have an apparent size of ~ 3 px. At the same time, the particles are not optimized to effectively scatter the laser light (e.g. the tungsten-carbide particles are of a dark gray color) and appear at about the same brightness as the tracers. A phase separation by their recorded size or intensity on the particle camera image is thus not possible. Instead, to obtain an image of only the particles, tracers are identified on the tracer camera image and the corresponding position is masked from the particle camera image. A detailed account of this method can be found in [30]. To verify the accuracy of the simultaneous measurement of particle and tracer behavior, the experiments are repeated without tracers for each particle population. In this case, the particles can be tracked directly on the particle camera image without biases due to the tracer removal method. No changes in the results were observed between the experimental runs with and without tracers.

One important prerequisite is that the images of the two cameras coincide with one another within ±1 px. This is achieved by calibrating both cameras using a target plate and by applying a self-calibration algorithm [31] to eliminate remaining disparities. The spatial resolution of the images is between 73 µm/px and 89 µm/px, mapping areas of 124 mm×170 mm to 158 mm×210 mm.

The image acquisition and synchronization between the cameras and the laser sheet are performed using the DaVis software by LaVision. Images are recorded as double-frames where two pictures are taken in quick succession with a time step between 5 ms and 30 ms (depending on the expected particle speed), resulting in an average particle displacement of 6 px. Successive double-frames are then acquired at a slower sampling frequency of 2 Hz to 15 Hz. This approach does not allow for a continuous tracking of individual particles over multiple time steps. However, it ensures that the images are statistically independent of each other in terms of the viscous timescale $d_{\mathrm{p}}^2/\nu < 50$ ms.

Figure 2 shows the typical timeline of an experimental run, here with the particle population CER 075-090 (how these data are obtained is discussed in the next section III C). The histogram of the vertical particle velocity v_z for each time step t is displayed in figure 2(a) as color plot. At $t = 0$ s the particle seeding is started. After some time ($t \approx 35$ s) the first particles arrive in the camera field of view, visible as a high count of particles around $v_z \approx -12$ mm/s. Alongside the particles, the fluid is accelerated downwards as can be seen in figure 2(b), where $\langle u_x \rangle_{\mathrm{FOV}}$ and $\langle u_z \rangle_{\mathrm{FOV}}$ are the fluid velocity in horizontal and vertical directions, respectively, averaged over the whole field of view. The initial particle front is generally very dense and establishing a strong downward draft that drags subsequent particles along in its wake. This causes an increase of the settling speed to $v_z \approx -20$ mm/s at $t \approx 60$ s. The exact nature of this transient process is not the object of this article and is left for future investigations. However, it is apparent that the particles cannot transfer enough energy to the fluid in order to uphold this fast settling state and the system slows down, reaching a stationary plateau (vertical dashed lines in figures 2(a) and (b)). This time interval, in which the settling particles and the induced flow have reached an equilibrium state, is the central focus of the present study. Finally, the seeding is stopped at $t = 160$ s and the image acquisition ends before the last particles reach the camera field of view.

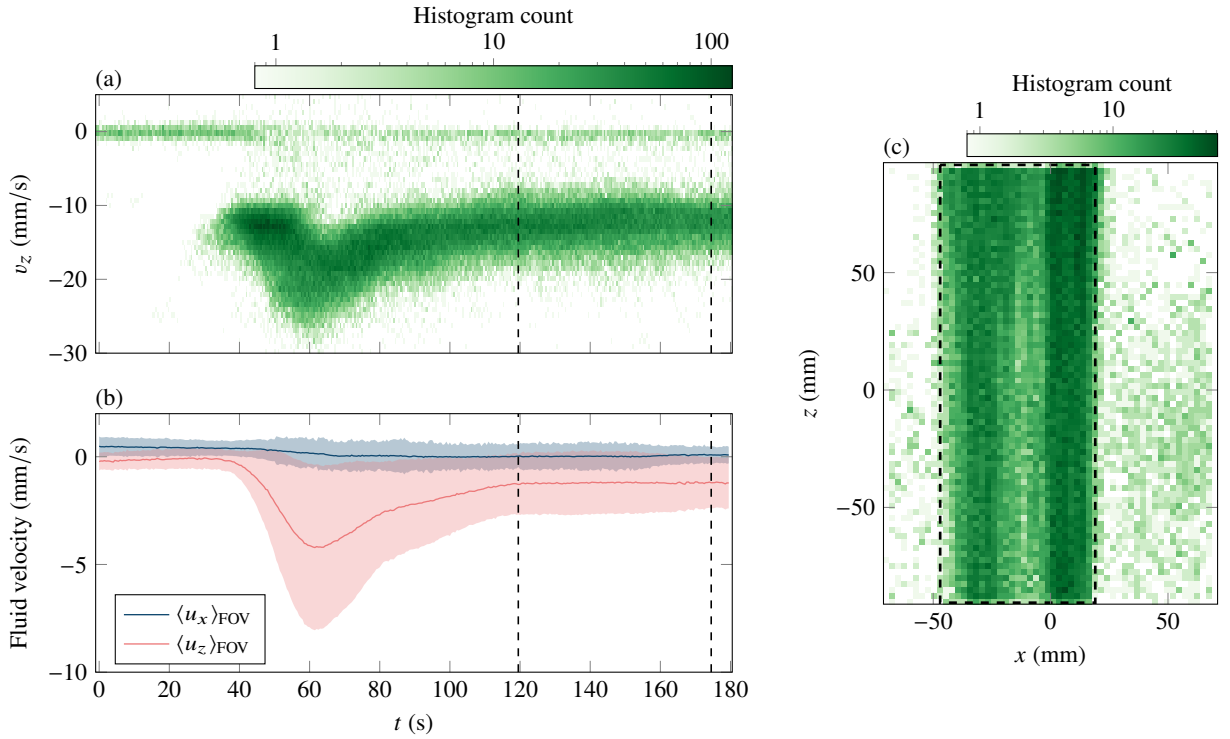

Figure 2: Timeline of an experimental run with the particle population CER 075-090. (a) Temporal histogram of the vertical particle velocity v_z. (b) Horizontal and vertical fluid velocity $\langle u_x \rangle_{\mathrm{FOV}}$ and $\langle u_z \rangle_{\mathrm{FOV}}$, respectively, averaged over the whole field of view. The shaded areas of the same color indicate their standard deviation. The particle seeding starts at $t = 0$ s and ends at $t = 160$ s. A stationary plateau for this experimental run is defined between $t = 119.5$ s and 147.5 s (vertical dashed lines). (c) Particle presence histogram over the plateau marked in (a) and (b). The position of the region of interest is marked by a dashed rectangle.

C. Data processing

To improve the signal-to-noise ratio of the recorded images, a minimal image is calculated over the whole experimental run and subtracted from each image. The horizontal and vertical fluid velocity fields $u_x(x, z, t)$ and $u_z(x, z, t)$ are calculated from the tracer camera images by performing particle image velocimetry (PIV) using DaVis. The interrogation window size is either 16 px × 16 px or 32 px × 32 px resulting in a spatial PIV resolution of 0.58 mm to 2.8 mm. As the fluid movement is slower than the particles, the tracer displacement is also lower, on average 0.7 px between frames. Potential tracers in the particle camera image are removed as described above [30] and the particle positions and velocity are extracted from the resulting image by particle tracking velocimetry (PTV). The PTV algorithm by Crocker, Grier, and Weeks [32] is used in its Matlab implementation by Blair and Dufresne [33].

For each experimental run, stationary plateaus are identified as time intervals in which the average particle and fluid dynamics do not change. The particle plume rarely occupies the whole width of the camera field of view. For example, figure 2(c) shows the histogram of all particle positions during the plateau marked in figure 2(a) and (b) (the histogram bin size is the same as the spatial PIV resolution). The plume is concentrated on a horizontal interval $-50\,\mathrm{mm} \lesssim x \lesssim 20\,\mathrm{mm}$. To exclude the areas of very low particle concentration outside the plume, a region of interest (ROI) is specified (displayed as a dashed square). Any particle and fluid statistics in the present study are determined within the stationary plateaus and their corresponding region of interest, if not stated otherwise. Averages of any quantity q over a plateau and its associated region of interest are denoted by an overbar $\bar{q}$. For PIV data, this amounts to an average over space and time, while PTV data is averaged over all particles that are detected within the region of interest during the time interval of the plateau. Each plateau consists of at least 1000 statistically independent tracked particles with 60 % of plateaus exceeding 10 000 particles. The total number of PIV vectors in the region of interest, accumulated over each plateau, ranges from 10^5 to 10^7. Spurious PIV vectors are excluded from statistics of the fluid velocity field, and interpolated from surrounding vectors when determining the local fluid velocity at a particle's position using natural-neighbor interpolation.

An intrinsic bias of this measurement procedure is that the laser sheet illuminates only one vertical plane. Depending on how

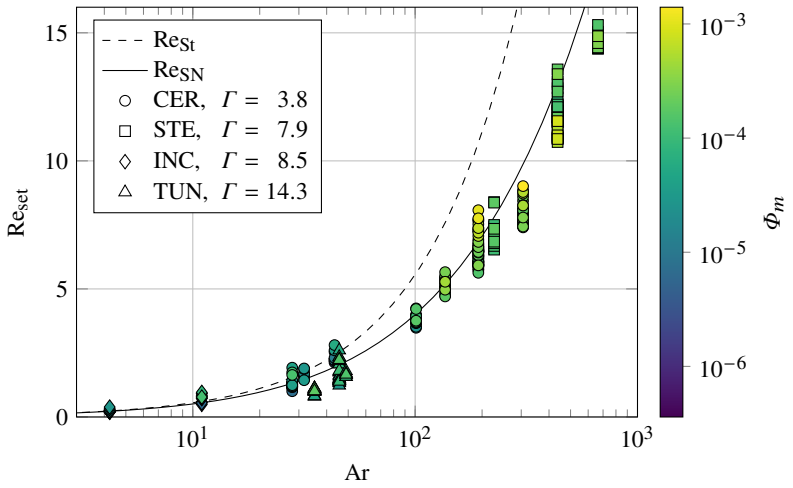

Figure 3: Settling Reynolds number $\mathrm{Re}_{\mathrm{set}}$ averaged over each plateau and region of interest vs. Archimedes number Ar. The marker shape denotes the particle material and the color scale gives the mass fraction Φ_m. The lines show the terminal Reynolds numbers for the Stokes drag ($\mathrm{Re}_{\mathrm{St}}$, dashed) and Schiller-Naumann drag ($\mathrm{Re}_{\mathrm{SN}}$, solid).

the particles fall and the flow in the tank develops, the plume may not be perfectly centered and may fall slightly besides the laser sheet. Then, the recorded particles and tracers are from the outer parts of the plume. This results in an additional scatter of the data (e.g. lower particle concentrations than in the centerline of the plume), though they still show distinct trends as will be demonstrated in the following section IV. Additionally, locally conditioned data are less affected by this bias, for instance the slip velocity in section IV C.

In the particle velocity histogram in figure 2(a), a small number of slow moving particles can be seen around $v_z = 0\,\mathrm{mm/s}$. These are likely leftover tracers that were not successfully removed from the particle camera image or contaminates from the water or particle population. As they are clearly separated by their vertical velocity magnitude from the faster falling particles, they are excluded from any subsequent calculations by setting a threshold velocity.

The number of particles N_p (not to be confused with the plume number) is determined by counting the detected particles (that are not excluded by the aforementioned velocity filter) within the region of interest of the first particle camera frame. The region of interest volume V_ROI is its area on the camera image multiplied by the laser sheet thickness of 2 mm. The loading is then characterized by the particle volume fraction $\Phi_V = N_\mathrm{p} V_\mathrm{p}/V_\mathrm{ROI}$ or the particle mass fraction $\Phi_m = \Gamma\Phi_V/(1+(\Gamma-1)\Phi_V)$. In the case of $\Phi_V \ll 1$ and $\Gamma\Phi_V \ll 1$, this formula simplifies to $\Phi_m \approx \Gamma\Phi_V$ (i.e., for small volume *and* mass fractions). The present experiment fulfills these conditions with $\Phi_V < 4\times10^{-4}$ and $\Gamma\Phi_V < 2\times10^{-3}$. In the following, we will mainly use the mass fraction Φ_m to quantify the particle loading, as it is more relevant to the investigated particle-fluid interaction than the purely geometric volume fraction.

IV. RESULTS

The following sections discuss the experimental results of the particle settling velocity in the laboratory frame of reference, the fluid velocity and turbulence induced by the particle plume, as well as the slip velocity of the particles with respect to the surrounding fluid. We also summarize our studies on the particle concentration.

A. Particle velocity

The particle settling velocity $\bar{v}_z$ of each plateau is calculated as an average of the vertical particle velocity v_z. Since $\Gamma > 1$ for all used particles, the sign of $\bar{v}_z$ is always negative (i.e., downwards). The corresponding settling Reynolds number $\mathrm{Re}_{\mathrm{set}} = |\bar{v}_z| d_\mathrm{p}/\nu$ is plotted over the Archimedes number Ar of the respective population in figure 3. For comparison, the terminal Reynolds numbers are plotted using Stokes drag (dashed line) and Schiller-Naumann drag (solid line). All experimental data for different particle materials (marker shape) collapse on roughly the same curve that closely follows the Schiller-Naumann prediction. The Stokes terminal Reynolds number is an acceptable reference only for the smallest $\mathrm{Ar} < 30$, where $\mathrm{Re}_{\mathrm{set}} < 2$ is small enough that both drag models result in similar terminal velocities. For high Ar, the Stokes model underestimates the drag acting on the particles which results in an overestimation of the terminal velocity. Consequently, the Schiller-Naumann terminal velocity v_SN

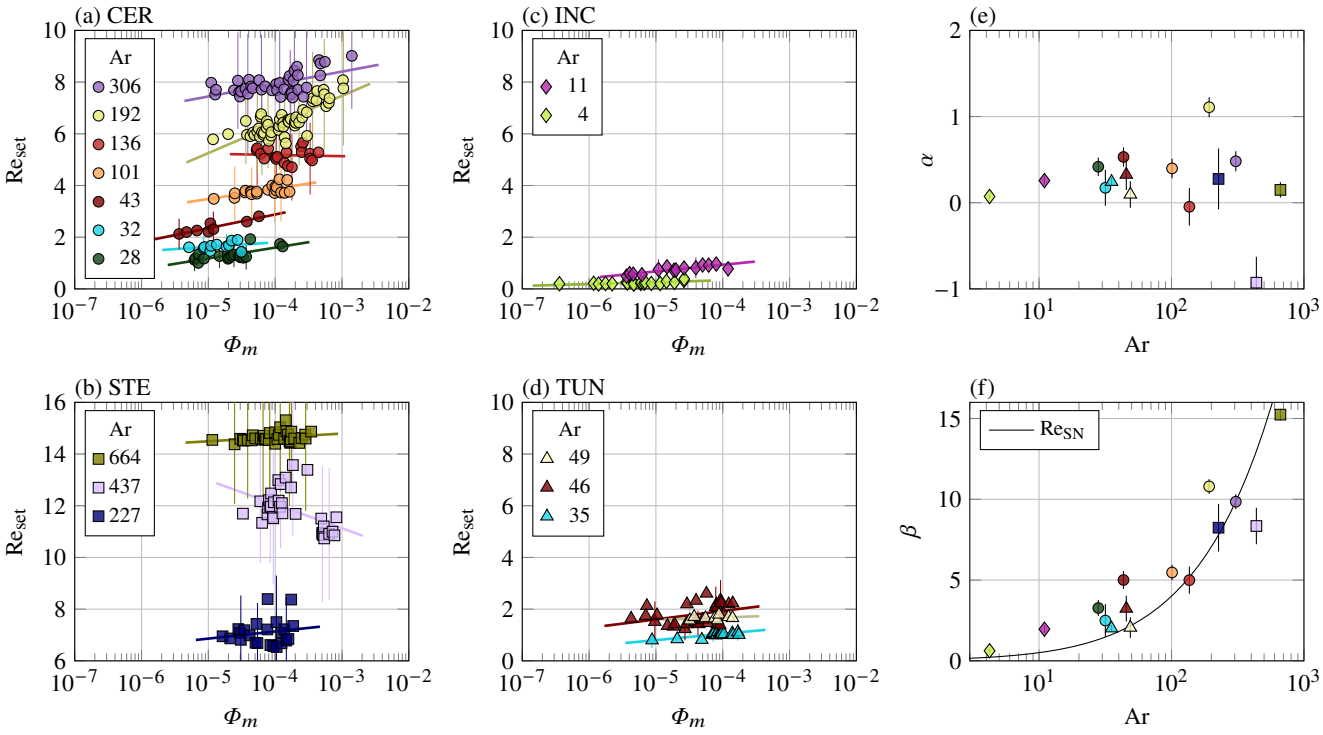

Figure 4: (a)–(d) Settling Reynolds number $\mathrm{Re}_{\mathrm{set}}$ vs. the particle mass fraction Φ_m. The data for CER, STE, INC and TUN particles are separated into the respective subplots for better visibility. Solid lines are fits of the function $\alpha \log_{10}(\Phi_m) + \beta$ to each particle population of the same color. (e)–(f) Values of the fit parameter α and β vs. Archimedes number Ar. The marker shape and color are the same as the corresponding population in the subplots (a)–(d). $\mathrm{Re}_{\mathrm{SN}}(\mathrm{Ar})$ is plotted in (f) as solid line for comparison with β. Error bars indicate the standard deviation of the data. In (a)–(d), error bars are shown for every fifth data point only.

will be used as reference velocity in the rest of this article. It should be noted that $\mathrm{Re}_{\mathrm{set}}$ uses the particle settling speed in the laboratory system, while $\mathrm{Re}_{\mathrm{SN}}$ is based on the slip velocity. A more in-depth analysis of the drag model is performed in section IV C.

While the Schiller-Naumann model predicts the general trend of the settling particles, the data in figure 3 shows a large scatter in $\mathrm{Re}_{\mathrm{set}}$ for the same Ar. This spread is in part caused by the different particle mass fractions Φ_m (marker color) for each experimental run. To more clearly show this dependency, figure 4 plots $\mathrm{Re}_{\mathrm{set}}$ over Φ_m. In general, the data show an increase of the settling speed for higher loading. To illustrate this progression with Φ_m and to guide the eye, the function $\mathrm{Re}_{\mathrm{set}} \simeq \alpha \log_{10}(\Phi_m) + \beta$ is fitted to each population and plotted as lines of the same color. The slope α in figure 4(e) does not show a clear dependence on Ar. While the data scatters strongly (and in the case of Ar = 136 (CER) and 437 (STE) even negative slopes are obtained), the effect of Φ_m on the settling velocity seems in general independent of Ar with an average slope of $\langle\alpha\rangle = 0.25$. The intercept β in figure 4(f) consequently has to contain the effect of Ar on $\mathrm{Re}_{\mathrm{set}}$. Indeed, it recovers the scaling of the settling Reynolds number with the Schiller-Naumann terminal Reynolds number $\beta \propto \mathrm{Re}_{\mathrm{SN}}(\mathrm{Ar})$ (solid line) already established in figure 3. These results are a first indication that the influence of the particle loading on the settling can be seen as independent of Ar as a first order approximation in the very dilute regime (i.e., $\Phi_V, \Phi_m \ll 1$). The same conclusion is drawn in the following sections where the fluid flow and slip velocity data are investigated.

Comparing the results in figure 4 with the Richardson-Zaki law (2), they exhibit an exact opposite trend: increased settling speed with higher loading (as stated in section III C, Φ_V in the Richardson-Zaki law can be replaced by Φ_m/Γ for the present experiments). This is not surprising, since the Richardson-Zaki law is derived for homogeneously distributed particles with an upwards return flow everywhere, while for the present experiment the fluid organizes into a large-scale recirculation with a downward flow in the region of the localized particle plume (see next section IV B). However, the basic scaling of $\bar{v}_z$ with the terminal velocity is still observed (figure 3). This discussion is further expanded in section IV C on the slip velocity.

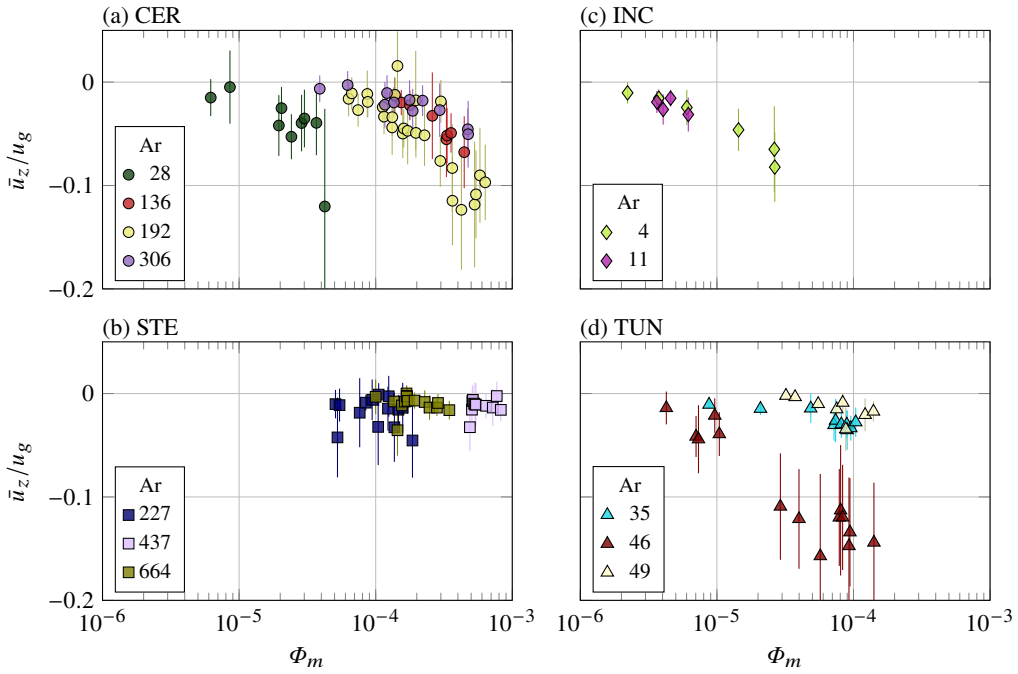

Figure 5: Vertical fluid velocity $\bar{u}_z$ normalized by the free-fall velocity u_g vs. the particle mass fraction Φ_m. The data for CER, STE, INC and TUN particles are separated into the subplots (a) to (d), respectively, for better visibility. The error bars indicate the standard deviation of the data.

B. Fluid velocity

As was shown in figure 2(b), the falling particles induce a flow into the fluid: the drag force transfers kinetic energy from the particles to the fluid and generates a down-flow in the region of the particle plume and an upwards return flow in the rest of the closed tank. The main question here is, how effective this energy transfer is and how strong the induced flow becomes. We thus present fluid velocity statistics (time and space averages as well as fluctuations in both directions), turbulence rates and dissipation rates in order to characterize as much as possible the particle induced flow.

Figure 5 shows the average vertical fluid velocity $\bar{u}_z$ over the particle mass fraction Φ_m. They are normalized by the free-fall velocity $u_g = \sqrt{|\Gamma - 1| g d_\mathrm{p}} = \sqrt{\mathrm{Ar}}\,\nu/d_\mathrm{p}$. This is the speed a fluid element with a density difference of $\Gamma - 1$ towards its surrounding would obtain if its potential energy over a distance of d_p was completely converted to kinetic energy (i.e., if drag was neglected). It thus represents a maximal possible fluid velocity due to the buoyancy forces generated by the particle. As the region of interest encloses the particle plume, the vertical fluid velocities are predominantly negative (i.e., downwards). It can be seen that for each population there is a general trend towards stronger flows with increasing loading. This is not surprising since a larger number of particles is accompanied with an increased input of energy into the fluid. Conversely, towards the very dilute case $\Phi_m \to 0$ the flow strength vanishes as the system approaches the reference case of a single particle settling in a still fluid. A clear trend with Ar is not discernible, though for most data, smaller Ar result in higher u_z/u_g for the same Φ_m. This would mean that with increasing Ar, the transfer of energy to the fluid becomes less efficient since the flow deviates further from the ideal conversion case of u_g. A more substantial demonstration of this effect is shown further below when the fluid velocity is compared to the velocity of the particles. Average velocities along the horizontal direction u_x are close to zero since no mean flow develops in this direction.

Due to the conservation of mass, the downward flow inside of the particle plume necessitates an upward return flow in the remainder of the tank. Taking the width of the region of interest as the diameter of a circular plume, the particles fall in an area of at most 4.3 % of the whole tank cross-section with a median value of 1 % throughout all experiments. Thus, while the return flow is not directly characterized by measurements, its speed is expected to be two orders of magnitudes slower than the fluid velocity inside the plume. Consequently, we expect the influence of the tank side walls on the plume properties to be negligible and that an increase of the tank dimensions do not affect the presented results.

The fluctuations u_i' of the fluid velocity components ($i = x, z$) are computed as $u_i'(\boldsymbol{x}, t) = u_i(\boldsymbol{x}, t) - \langle u_i \rangle_\mathrm{plat}(\boldsymbol{x})$, with the mean flow $\langle u_i \rangle_\mathrm{plat}$ being averaged over the time interval of the plateau for each position. The overall magnitude of u_i' is calculated as its root-mean-square (rms) average over the plateau and then averaged over the region of interest, denoted by $\overline{\mathrm{rms}}(u_i') \equiv \langle\, \mathrm{rms}_\mathrm{plat}(u_i') \,\rangle_\mathrm{ROI}$.

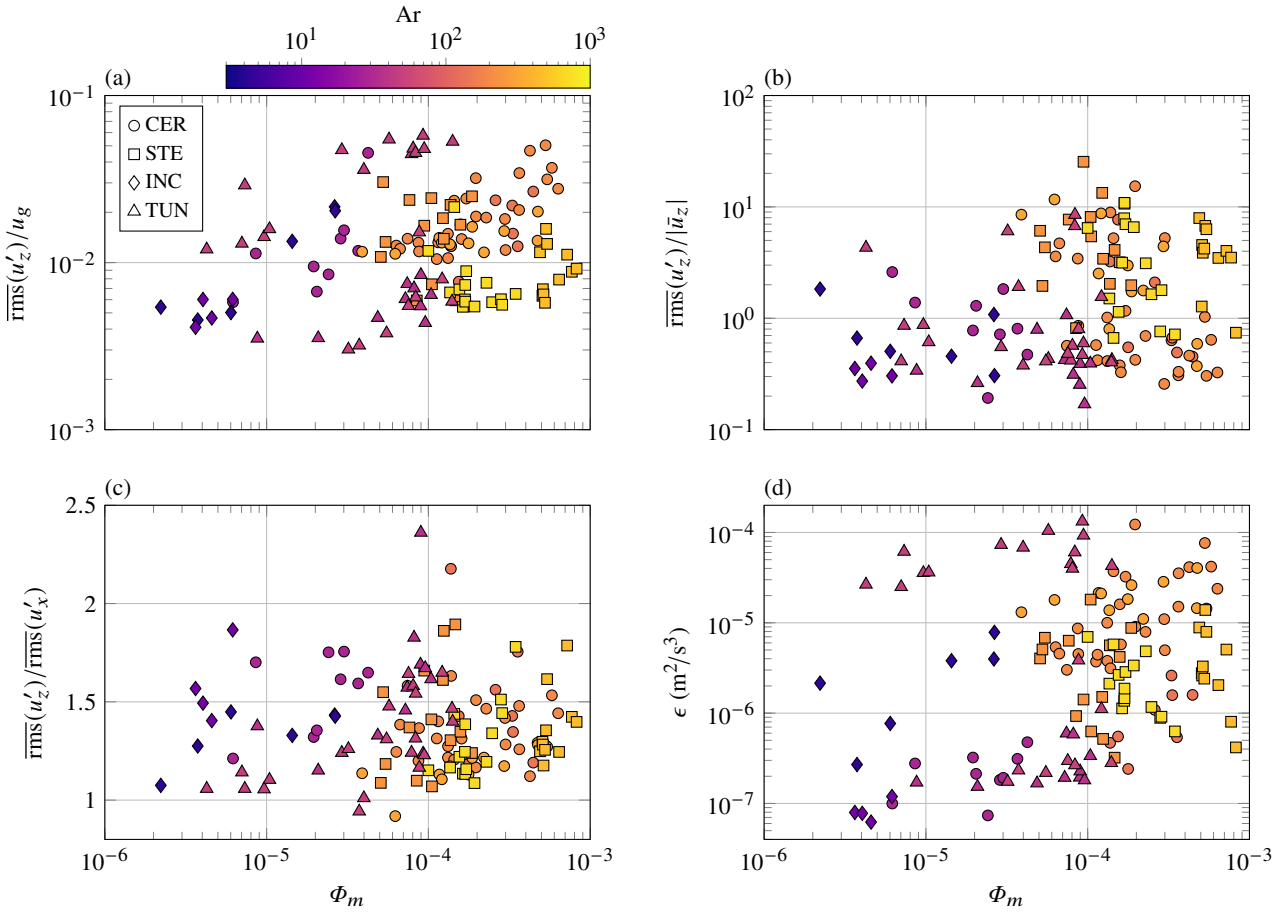

Figure 6: Fluid velocity fluctuations and associated turbulent quantities vs. the particle mass fraction Φ_m. The color codes the Archimedes number Ar. The marker shapes stand for the particle material. (a) Magnitude of the vertical fluid velocity fluctuations normalized by the free-fall velocity u_g. (b) Vertical turbulence rate. (c) Isotropy ratio. (d) Mean dissipation rate ϵ.

The vertical fluctuation magnitude is plotted in figure 6(a), normalized with the free-fall velocity u_g. It increases with the mass loading, similar to its average counterpart (figure 5), while no clear trend on Ar can be established. Normalizing the fluctuations by the respective mean flow gives the turbulence rate $\overline{\mathrm{rms}}(u_z')/|\bar{u}_z|$ in figure 6(b). For most plateaus, it lies between 0.2 and 20 showing that the flow can exhibit strong vertical fluctuations up to one order of magnitude above the downward mean flow. The mass loading does not seem to have any influence on these turbulent rates. On the other hand, higher Archimedes numbers Ar show a trend to stronger turbulence rates. This means that each particle transfers energy to the fluid individually, unaffected by the other particles surrounding it, and the split of energy transferred to the mean flow and the fluctuations is solely dictated by Ar. This conclusion is more clearly substantiated at the end of this section, where the fluid and particle kinetic energies are compared.

The horizontal and vertical fluctuations are compared by the isotropy ratio $\overline{\mathrm{rms}}(u_z')/\overline{\mathrm{rms}}(u_x')$ in figure 6(c). The vertical fluctuations are between 1 and 1.9 times larger than the cross-stream fluctuations, with an average value of 1.4. This shows that the turbulence is not quite isotropic. While the data scatter over a wide range, the settling particles consistently induce higher levels of fluctuation in the direction of the particle motion.

To characterize the fluctuating nature of the flow further, the mean energy dissipation rate ϵ is computed. Because of the special role of gravity in the experiment, the turbulence is assumed to be axisymmetric along z, i.e., the statistical properties of the horizontal velocity components are considered invariant under rotation around the vertical axis. Consequently, the properties of the unknown velocity component u_y are estimated using the known component u_x. The mean dissipation rate is then computed as [34]

$$\epsilon = \nu \left\{ -\overline{\left(\frac{\partial u_z'}{\partial z}\right)^2} + 2\overline{\left(\frac{\partial u_z'}{\partial x}\right)^2} + 2\overline{\left(\frac{\partial u_x'}{\partial z}\right)^2} + 8\overline{\left(\frac{\partial u_x'}{\partial x}\right)^2} \right\} . \tag{3}$$

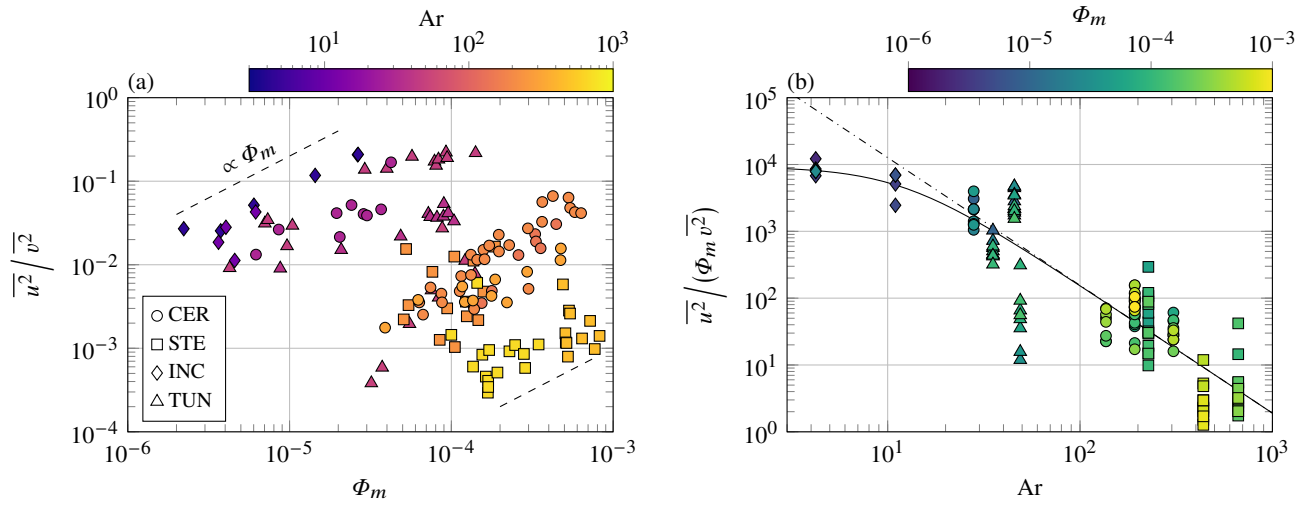

Figure 7: (a) Ratio of average squared fluid- and particle-velocities vs. mass fraction Φ_m. The dashed lines indicate a linear scaling with Φ_m. (b) Compensated squared velocity ratio vs. Archimedes number Ar. The solid line in is a fit of the function $\xi/(1+\lambda \mathrm{Ar}^{\kappa})$ with an asymptotic power law (dash-dotted line) towards high Ar.

Once again, the overbars denote averages over the plateau (time) and the region of interest (space). The velocity gradients are calculated using a central finite difference scheme between adjacent velocity vectors of the PIV grid. The resulting data of ϵ is plotted in figure 6(d). They range from $\sim 10^{-7}\,\mathrm{m^2/s^3}$ up to $10^{-4}\,\mathrm{m^2/s^3}$ and tend to increase with mass loading and Archimedes numbers. Using this data, the Kolmogorov length scale $\eta = (\nu^3/\epsilon)^{1/4}$ ranges from 0.3 mm to 2 mm which is between 0.63 to 2.6 times the size of the PIV interrogation window. This spatial resolution is enough to reach about 90 % of the real value of dissipation rate [35–37].

To investigate the transfer of energy to the large-scale flow more closely, the relationship between particle and fluid velocities is investigated. Figure 7(a) shows the loading-dependency of the ratio $\overline{u^2}/\overline{v^2}$ of the averaged squared velocity magnitudes of the fluid $\overline{u^2} = \overline{u_x^2 + u_z^2}$ and the particles $\overline{v^2} = \overline{v_x^2 + v_z^2}$. These quantities characterize the kinetic energies of the two phases. For the same Ar (color), the data shows a linear dependence on the mass fraction (dashed lines). This simply means, that an increase in the number of particles causes a similar increase in the amount of transferred energy. As a consequence, the ratio of the rms velocities $\overline{\mathrm{rms}}(u)/\overline{\mathrm{rms}}(v) = \left(\overline{u^2}/\overline{v^2}\right)^{1/2}$ is approximately proportional to $\sqrt{\Phi_m}$. The linearity might disappear at higher mass fractions than presented here ($\Phi_m > 10^{-3}$), once local particle-particle interactions become relevant. At the same time the ratio decreases with increasing Ar without affecting the linearity in Φ_m. While $\overline{v^2}$ increases with Ar due to faster settling velocities (see the following section and figure 3), a smaller fraction of that energy is transferred to the fluid.

To detail this progression further, figure 7(b) shows the squared velocity ratio compensated by Φ_m. Towards low Ar, the compensated velocity ratio appears to reach a constant plateau, while towards high Ar it drops off by multiple orders of magnitude. The transition between these regions at Ar $\sim$ 20 coincides with the end of the Stokes regime (see figure 3). This suggests that the decrease in transferred energy is caused by a change of the flow around the particles. In the Stokes regime, the viscosity-dominated creeping flow is most efficient at converting particle energy into kinetic energy of the flow. Since the flow structure around a particle does not change for $\mathrm{Re_p} \lesssim 1$, the squared velocity ratio can be expected to be constant. However, with increasing Archimedes number the local flow starts to be influenced by inertial effects, leading to the detachment of the boundary layer and recirculation zones in the wake. This transition towards a flow that is less dominated by viscosity is a likely cause for the reduced energy transfer efficiency. To quantify this progression of the squared velocity ratio with Ar, the function $\xi/(1+\lambda \mathrm{Ar}^{\kappa})$ is fitted to the data (solid line in figure 7(b)). The constant level at small Ar has a value of $\xi = (9.2 \pm 4.4) \times 10^3$, while for large Ar, the function approaches a power law $(\xi/\lambda)\mathrm{Ar}^{-\kappa}$ with $\lambda = (1.1 \pm 0.9) \times 10^{-2}$ and $\kappa = 1.85 \pm 0.10$ (dash-dotted line). The choice of a power law is not theoretically motivated and it is likely that for even higher Ar, the squared velocity ratio has a complex progression as the flow around the particles becomes more complicated at higher Reynolds numbers. Similarly, the predicted plateau for low Ar is not yet clearly visible in the present data and requires additional experiments with particles of Ar < 4.

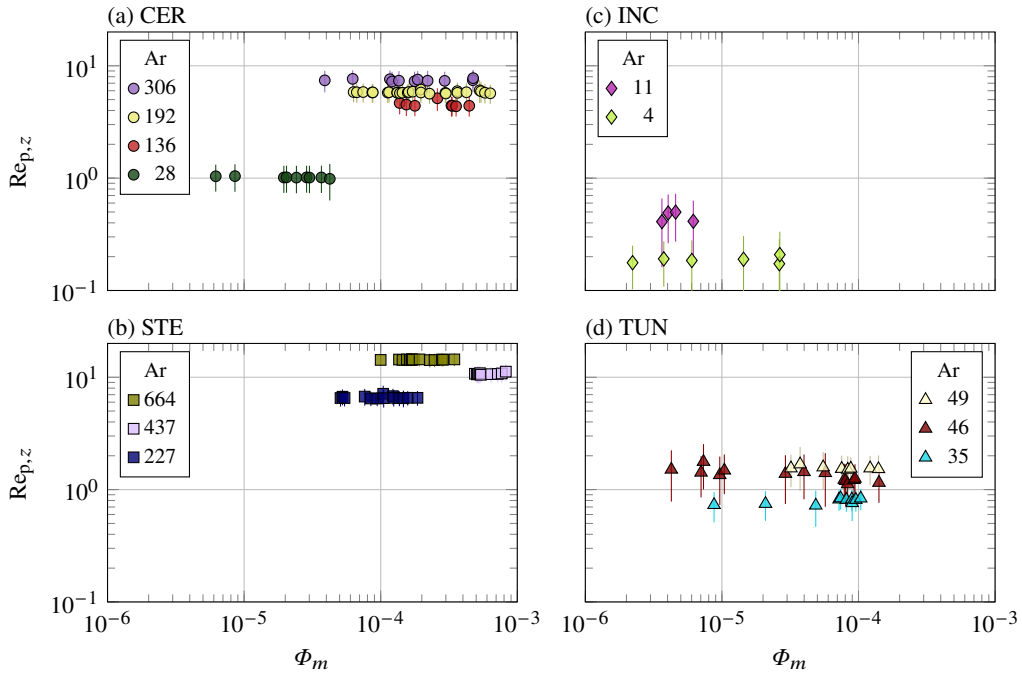

Figure 8: (a)–(d) Particle Reynolds number $\mathrm{Re}_{\mathrm{p},z}$ vs. mass fraction Φ_m for CER, STE, INC and TUN, respectively. Error bars indicate the standard deviation of the data.

C. Slip velocity

As described previously, the slip velocity $\Delta\boldsymbol{v} = \boldsymbol{v} - \boldsymbol{u}|_\mathrm{p}$ is the governing quantity for the drag acting on a particle (section II). In the present experiment, $\boldsymbol{u}|_\mathrm{p}$ is evaluated by selecting the PIV vector that is closest to the particle position. Figure 8 shows the particle Reynolds number calculated from the average vertical slip velocity $\mathrm{Re}_{\mathrm{p},z} = |\overline{\Delta v_z}|d_\mathrm{p}/\nu$ over the mass fraction Φ_m. For all populations, $\mathrm{Re}_{\mathrm{p},z}$ is remarkably independent of the particle loading. The slight downward trend of the TUN population with Ar = 46 (figure 8(d)) is within the standard deviation of the data. This is very much an outlier and we refrain from assigning it further significance as for all other Ar the independence from Φ_m persists. This means, that for all of the presented mass fractions $\Phi_m < 10^{-3}$ (and correspondingly $\Phi_V < 3 \times 10^{-4}$), particles do not interact with one another – neither directly (particle-particle interaction) or indirectly through their wake (local particle-fluid-particle interaction). In turn, this also means that any modification of the settling velocity $\bar{v}_z$ by the particle loading (see figure 4) is exclusively mediated by the large-scale fluid flow (section IV B). This can be interpreted as a *global* particle-fluid-particle interaction, where the collective induction of a global fluid flow by all preceding particles influences the settling of the subsequent particles.

Each population in figure 8 has its own level of $\mathrm{Re}_{\mathrm{p},z}$, which increases with Ar. As already discussed in figure 3 for Re_set, this progression follows the predictions of the Schiller-Naumann drag model. To verify this, the left- and right-hand sides of equation (1) are plotted against one another in figure 9(a). All the data closely follow the theoretical prediction (dashed line), but have consistently higher values of $\mathrm{Re}_{\mathrm{p},z} f_\mathrm{SN}(\mathrm{Re}_{\mathrm{p},z})$. This is shown more clearly in the compensated plot of $\mathrm{Re}_{\mathrm{p},z}/\mathrm{Re}_\mathrm{SN}$ over Ar in figure 9(b). For almost all populations, $\mathrm{Re}_{\mathrm{p},z}$ falls into an interval of (80 ± 10) % of the Schiller-Naumann terminal Reynolds number (gray shaded area) over the whole Ar-range. Only the TUN particles show a different behavior with $\mathrm{Re}_{\mathrm{p},z}/\mathrm{Re}_\mathrm{SN} \sim (60 \pm 15)$ %. Nonetheless, for all populations the reduced slip velocity with respect to the terminal velocity indicates a hindering of the settling relative to the surrounding fluid. The strongly increased scatter of the data from the previously very small spread in figures 8 and 9(a) indicates that the Schiller-Naumann prediction compensates the Ar and Φ_m dependence of the slip velocity very well.

The terminal velocity is calculated by assuming a completely quiescent fluid, i.e., all the energy transferred to the fluid by drag is dissipated in the particle's boundary layer. As demonstrated by the present experiments, this is not the case for a continuous plume of settling particles. During the stationary plateau, the loss of energy by the particles through drag has to balance not only the local dissipation within their individual boundary layer but also the global dissipation in the large-scale recirculation flow. The 20 % reduced slip velocity with respect to the Schiller-Naumann terminal velocity is interpreted as a consequence of this additional contribution.

By definition, the settling velocity is the sum of the slip and fluid velocities. Since the values of Re_set spread around Re_SN (see figure 3), the fluid velocity has to be of similar magnitude as the difference between slip velocity and v_SN. Figure 5 showed that

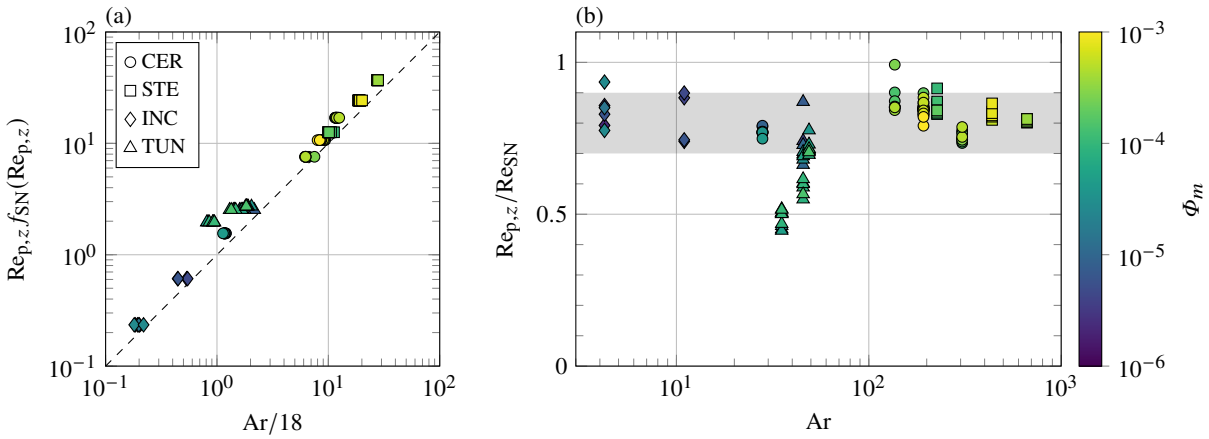

Figure 9: (a) Validation of the Schiller-Naumann drag law by plotting $\mathrm{Re}_{\mathrm{p},z} f_{\mathrm{SN}}(\mathrm{Re}_{\mathrm{p},z})$ vs. $\mathrm{Ar}/18$. The dashed line marks the theoretical prediction (1). (b) Particle Reynolds number $\mathrm{Re}_{\mathrm{p},z}$ normalized by the Schiller-Naumann terminal Reynolds number $\mathrm{Re}_{\mathrm{SN}}$ vs. Archimedes number Ar. Marker shape and color indicate the material and mass fraction Φ_m, respectively. The gray shaded area marks the common interval for all materials except a portion of the TUN data.

the fluid speed increases with higher mass fractions, while the slip velocity and Schiller-Naumann prediction are independent of Φ_m (figure 8 and equation (1)). It is thus mainly a question of how many particles need to be added to the system, before the induced fluid flow can compensate for the hindering observed for the slip velocity.

As stated before in section IV A, the Richardson-Zaki law (2) considers the settling velocity v_z for homogeneously distributed particles. Richardson and Zaki [23] estimated the constant upwards return flow speed as $u_{\mathrm{RZ}} = -v_z \Phi_V/(1-\Phi_V)$ which would be negligible for the present loadings ($|u_{\mathrm{RZ}}/v_z| \approx \Phi_V < 4 \times 10^{-4}$). Thus, the settling velocity v_z in the Richardson-Zaki law can be identified with the slip velocity Δv_z for $\Phi_V \ll 1$ and can be compared with the data in figure 8. The furthest deviation from unity of the factor $(1-\Phi_V)^n$ in the Richardson-Zaki law for the parameters of the present experiments is 0.9986 (less than 0.2 %), which agrees with the observation that the slip velocity is independent of the particle loading. The pre-factor γ would then be identified with the ratio $\mathrm{Re}_{\mathrm{p},z}/\mathrm{Re}_{\mathrm{SN}}$. The previously reported values of $\gamma \approx 0.8$ to 0.9 [26] are within the upper range of hindering observed in figure 9(b) with $0.7 \lesssim \mathrm{Re}_{\mathrm{p},z}/\mathrm{Re}_{\mathrm{SN}} \lesssim 0.9$ (again, the TUN particles deviate from this behavior). This illustrates that the return flow in a homogeneously distributed particle suspension loses its relevance at low loadings since no structured flow is established. In contrast, for a localized plume the induced large-scale recirculation influences the settling velocity even down to $\Phi_m \sim 10^{-6}$ (figure 4), corresponding to $\Phi_V \sim 10^{-7}$.

D. Local Particle concentration

The particle settling alterations with respect to the reference case of isolated particles falling in a fluid at rest we have shown in the previous section could be linked to preferential sampling of the flow or to collective effects as those resulting in settling enhancement in turbulent flows [38, 39]. In section IV C, we have argued that global particle-fluid-particle interactions, through the initiation of the large scale recirculation, were responsible for the settling enhancement we measure. Nonetheless, we have performed a thorough concentration analysis based on a Voronoi analysis [40, 41]. This way, we have access to the local particle concentration around each particle, global clustering indicators as well as statistics of any quantity conditioned on the local particle concentration. The global indicators show that we never measure any clustering in the flow. The conditioning of various fluid and particle statistics on the local particle concentration confirms the latter has no influence on the results presented in the previous sections.

V. DISCUSSION AND CONCLUSIONS

We have studied the free fall of particles in an initially quiescent fluid for a wide range of the parameter space: density ratio Γ ranging from 4 to almost 15, Archimedes number Ar spanning two and mass loading three orders of magnitude. According to the Reynolds numbers of the studied particles, the relevant drag law is expected to change from Stokes regime for lower particle Reynolds numbers around 1 to non-linear regimes as described by the Schiller-Naumann model for higher values, up to 15 for the present data. We have shown that the settling particles roughly follow v_{SN} (figure 3 and 9), the terminal velocity of an isolated

particles submitted to Schiller-Naumann drag. Higher mass fractions increase the settling velocity through a stronger induced background flow (figure 4), while the particle slip velocity is entirely unaffected (figure 8).

The energy transfer between the two phases has several origins. The falling particles induce a downward flux of momentum that is compensated by an upward fluid motion to ensure a vanishing net flow rate. As particles are injected at the center of a wide water tank, the upward fluid motion is occurring as a large-scale recirculation in regions free of particles. In turn, the fluid is flowing downward around the particle plume. A transfer of momentum from the particles to the fluid can also occur by direct entrainment of the fluid surrounding the falling particles. Finally, local energy transfers from and to the fluid can occur in close vicinity of each particle.

The ratio of the streamwise to crosswise velocity fluctuations in the core of a monophasic jet is about 1.4 ([42] and references therein). Studies of particle-induced flows report higher values of this ratio. Bordoloi *et al.* [11] found 1.6 in the center of a plume of particles with $\Gamma = 2$, $d_\mathrm{p} = 2\,\mathrm{mm}$, $\mathrm{Ar} = 8 \times 10^4$ and $\Phi_m = 0.2$. In contrast, Parthasarathy and Faeth [27, 43] found 2.0 ± 0.2 for homogeneously distributed particles with $\Gamma = 2.45$, $d_\mathrm{p} = 0.5\,\mathrm{mm}$ to $2\,\mathrm{mm}$, $\mathrm{Ar} = 10^3$ to 10^5 and $\Phi_m = 4 \times 10^{-5}$ to 3×10^{-4}. Values between 1.9 and 2.1 were also reported for a plume of rising bubbles [44]. Parthasarathy and Faeth [27] attribute the strong anisotropy of the velocity fluctuation in their experiments to the combined effects of the particle motion and wake, which both occur in the streamwise direction. It has to be emphasized that they study particles that are evenly distributed throughout the fluid, which forces the counterflow to occur where the particles fall, further increasing the magnitude of the streamwise velocity fluctuations in the fluid. In the present experiments, the ratio of streamwise to cross-stream velocity fluctuations lies at about 1.4 (figure 6(c)), which is close to the values observed for monophasic fluid jets. This indicates that the fluid fluctuations disassociate from the local fluctuations of the particle wakes in part since fluid is accelerated outside the region of interest and then entrained into the plume. While the particle wakes might contribute to the scatter of the isotropy ratio, their local effect is evidently small compared to the collectively induced large-scale flow. As the particles settle just outside the laminar Stokes regime ($\mathrm{Re}_{\mathrm{p},z} < 15$, figure 8) their wakes are expected to be limited in space and not stretch far behind them. Combined with the low volume fractions they likely take up only limited space and are thus a secondary effect to the large-scale recirculation.

We estimate the turbulent energy dissipation rate from the fluctuations of the fluid velocity (figure 6(d)). Our largest values at $10^{-4}\,\mathrm{m^2/s^3}$ are three orders of magnitude smaller than that of Bordoloi *et al.* [11] ($\epsilon \approx 10^{-2}\,\mathrm{m^2/s^3}$), which is consistent with their much higher Ar and particle loading. On the other hand, the dissipation rates found by Parthasarathy and Faeth [27, 43] for homogeneously distributed particles cover a range of $2 \times 10^{-5}\,\mathrm{m^2/s^3}$ to $2 \times 10^{-4}\,\mathrm{m^2/s^3}$, despite their larger Ar at loadings similar to ours. This shows that the spatially organized flow created by a localized plume produces stronger fluctuations than the uniform counterflow of a homogeneous suspension at the same loadings and Archimedes numbers.

In the reference frame moving with the fluid the particle settling is hindered and the lost energy feeds the fluctuations of the induced flow. Still, as discussed in section IV B, the transition from Stokes drag to non-linear drag also explains the scaling change of this energy transfer. Among the mechanisms described above to explain the main transfers of energy from the particles to the fluid, the global flow rate scales with mass loading while the local particle to fluid energy exchange appears to be more efficient at lower Archimedes numbers presumably due to their viscosity-dominated boundary layer.

We have found that there was no clustering, no preferential concentration and no local concentration effects on any quantity of interest. This further confirms that all the settling alterations are solely due to global particle-fluid-particle interactions. Indeed, the particle plume induces a large-scale flow whose properties alter the behavior of subsequent particles, but particles present at a given time in a given region have no influence on their neighbors. It could also be of interest to study how higher and lower levels of confinement impact these findings.

In this study, we have paved the way for further work where turbulence will be forced: we have gathered results on the settling of particles but also on their back reaction on the fluid that will both be used as reference cases in upcoming experiments where a pre-existing fluid flow will be forced by two horizontally oscillating grids. It will be very informative to see if the efficiency transfer found in the present article remain valid in the turbulent case where preferential concentration and clustering may come into play.

ACKNOWLEDGMENTS

The authors would like to acknowledge Cindy Truong and Jerome Hemeret for their contributions on the velocity and turbulent quantities estimations and on the particle characterization. We are grateful to Tierry Pichon and Lahcene Cherfa for their constant help in the design, setup and maintenance of the experiment and Anne Dejoan for fruitful discussions. Last but not least, we thank Judith Vatteville from LaVision for her support in many aspects on configuring and evaluating the optical measurement system. This project has been funded by the French Direction Générale de l'Armement through two AID program grants.

Population	$(a/b)_{80}$	d_p (µm)	Ar	Material Specification	Supplier	№ Experiments no PIV	№ Experiments with PIV
CER 075–090	1.62	100.8 ± 18.2	28.0 ± 10.1	ZrO_2 (62 %)	A.M.P.E.R.E. alloys	10	9
CER 090–106	1.28	105.0 ± 14.0	31.7 ± 8.4	SiO_2 (28 %)		11	0
CER 106–125	1.34	116.7 ± 15.4	43.4 ± 11.5	Al_2O_3 (5 %)		8	0
CER 125–140	1.34	154.6 ± 23.2	101.0 ± 30.3	CaO (3 %)		21	0
CER 140–160	1.35	170.9 ± 26.9	136.4 ± 43.0	TiO_2 (< 1 %)		11	8
CER 160–180	1.36	191.6 ± 29.4	192.4 ± 58.9	Fe_2O_3 (< 1 %)		25	28
CER 180–200	1.19	223.6 ± 27.1	305.8 ± 74.1			29	11
STE 125–140	1.29	149.8 ± 17.5	226.6 ± 52.9	Stainless steel (similar to AISI 301)	A.M.P.E.R.E. alloys	9	14
STE 160–180	1.25	186.5 ± 22.0	437.3 ± 103.2			24	11
STE 180–200	1.25	214.4 ± 21.7	664.2 ± 134.6			23	15
INC 032–040	1.51	38.8 ± 7.8	4.2 ± 1.7	Metcoclad 625	Oerlikon Metco	13	6
INC 050–063	1.52	53.3 ± 13.5	11.0 ± 5.6			10	4
TUN 050–063	1.30	64.8 ± 7.1	35.3 ± 7.7	Amperit® 518 (WC-12Co)	H.C. Starck STC GmbH	12	10
TUN 063–075	1.31	70.5 ± 8.3	45.6 ± 10.7			14	14
TUN 075–090	1.32	72.2 ± 12.4	48.9 ± 16.8			0	8

Table II: Properties of the particle populations employed in the present experiment. The populations are identified by their material label (see table I) and the bounding sieve sizes in micrometer. $(a/b)_{80}$ is the 80th percentile of the particle elongation ratio with the major and minor diameter a and b of the circumscribed ellipse. The characteristic diameter d_p is the median value of the equivalent diameter distribution $d_{eq} = \sqrt{ab}$ and the given uncertainty is the standard deviation of the distribution with respect to the median. The Archimedes number Ar is calculated at 20 °C with its uncertainty propagated from d_p. The material specification of the particles is given as their chemical composition or their exact trade name as stated by their supplier. The number of experimental runs (№ Experiments) per population evaluated in this study are given separately for runs where no PIV was performed and for those with PIV.

Appendix: Particle population properties

Table II lists properties of the specific particle populations used in the present experimental study. The characteristic particle diameter d_p of most populations is higher than the upper sieve size, since the sieve openings are square and their diagonal allows for non-spherical particles of up to $\sqrt{2}$ larger size to pass. Additionally, long prolate particles may fit through a sieve if their minor axis is small enough.

[1] K. Gustavsson, M. Z. Sheikh, A. Naso, A. Pumir, and B. Mehlig, Effect of particle inertia on the alignment of small ice crystals in turbulent clouds, J. Atmos. Sci. **78**, 2573 (2021).

[2] J. T. Gilchrist and M. A. Jellinek, Sediment waves and the gravitational stability of volcanic jets, Bull. Volcanol. **83**, 64 (2021).

[3] L. Bourouiba, The Fluid Dynamics of Disease Transmission, Annu. Rev. Fluid Mech. **53**, 473 (2021).

[4] D.-H. Jeong, M. K. H. Lee, V. Thiévenaz, M. Z. Bazant, and A. Sauret, Dip coating of bidisperse particulate suspensions, J. Fluid Mech. **936**, A36 (2022).

[5] M. Kostoglou, T. D. Karapantsios, and O. Oikonomidou, A critical review on turbulent collision frequency/efficiency models in flotation: Unravelling the path from general coagulation to flotation, Adv. Colloid Interface Sci. **279**, 102158 (2020).

[6] S. Balachandar and J. K. Eaton, Turbulent Dispersed Multiphase Flow, Annu. Rev. Fluid Mech. **42**, 111 (2010).

[7] C. T. Crowe, J. D. Schwarzkopf, M. Sommerfeld, and Y. Tsuji, *Multiphase Flows with Droplets and Particles*, 2nd ed. (CRC Press, Boca Raton, 2012).

[8] L. Brandt and F. Coletti, Particle-Laden Turbulence: Progress and Perspectives, Annu. Rev. Fluid Mech. **54**, 159 (2022).

[9] S. E. Elghobashi and G. C. Truesdell, On the two-way interaction between homogeneous turbulence and dispersed solid particles. I: Turbulence modification, Phys. Fluids A **5**, 1790 (1993).

[10] É. Guazzelli, Sedimentation of small particles: How can such a simple problem be so difficult?, C.R. Mec. **334**, 539 (2006).

[11] A. D. Bordoloi, C. C. K. Lai, L. K. Clark, G. V. Carrillo, and E. A. Variano, Turbulence statistics in a negatively buoyant multiphase plume, J. Fluid Mech. **896**, A19 (2020).

[12] B. Metzger, M. Nicolas, and É. Guazzelli, Falling clouds of particles in viscous fluids, J. Fluid Mech. **580**, 283 (2007).

[13] A. C. H. Lai, R.-Q. Wang, A. W.-K. Law, and E. E. Adams, Modeling and experiments of polydisperse particle clouds, Environ. Fluid Mech. **16**, 875 (2016).

[14] Q. Kriaa, E. Subra, B. Favier, and M. Le Bars, Effects of particle size and background rotation on the settling of particle clouds, Phys. Rev. Fluids **7**, 124302 (2022).

[15] K. Papuga, J. Kaszubkiewicz, and D. Kawałko, Do we have to use suspensions with low concentrations in determination of particle size distribution by sedimentation methods?, Powder Technol. **389**, 507 (2021).

[16] S. Han, Z. Sun, Z. F. Tian, T. Lau, T. Lau, and G. Nathan, Particle velocity measurement within a free-falling particle curtain using microscopic shadow velocimetry, Opt. Express **29**, 10923 (2021).

[17] N. Mingotti and A. W. Woods, Stokes settling and particle-laden plumes: Implications for deep-sea mining and volcanic eruption plumes, Phil. Trans. R. Soc. A **378**, 20190532 (2020).

[18] C. K. Ho, J. M. Christian, J. E. Yellowhair, K. Armijo, W. J. Kolb, S. Jeter, M. Golob, and C. Nguyen, On-Sun Performance Evaluation of Alternative High-Temperature Falling Particle Receiver Designs, J. Sol. Energy Eng. **141**, 011009 (2019).

[19] R. Ansart, A. de Ryck, and J. A. Dodds, Dust emission in powder handling: Free falling particle plume characterisation, Chem. Eng. J. **152**, 415 (2009).

[20] B. R. Sutherland, B. Mueller, B. Sjerve, and D. Deepwell, Particle settling from constant-flux surface gravity currents and a near-stationary particle-bearing layer, Phys. Rev. Fluids **6**, 063802 (2021).

[21] É. Guazzelli and J. Hinch, Fluctuations and Instability in Sedimentation, Annu. Rev. Fluid Mech. **43**, 97 (2011).

[22] L. Schiller and A. Naumann, Über die grundlegenden Berechungen bei der Schwerkraftaufbereitung, Z. Ver. Dtsch. Ing. **77**, 318 (1933).

[23] J. F. Richardson and W. N. Zaki, Sedimentation and fluidisation: Part I, Trans. Inst. Chem. Eng. **32**, 35 (1954).

[24] R. Di Felice, The sedimentation velocity of dilute suspensions of nearly monosized spheres, Int. J. Multiphase Flow **25**, 559 (1999).

[25] P. N. Rowe, A convenient empirical equation for estimation of the Richardson-Zaki exponent, Chem. Eng. Sci. **42**, 2795 (1987).

[26] X. Yin and D. L. Koch, Hindered settling velocity and microstructure in suspensions of solid spheres with moderate Reynolds numbers, Phys. Fluids **19**, 093302 (2007).

[27] R. N. Parthasarathy and G. M. Faeth, Turbulence modulation in homogeneous dilute particle-laden flows, J. Fluid Mech. **220**, 485 (1990).

[28] M. Holmgren, X Steam, Thermodynamic properties of water and steam, https://uk.mathworks.com/matlabcentral/fileexchange/9817-x-steam-thermodynamic-properties-of-water-and-steam (2007).

[29] E. Loth, Drag of non-spherical solid particles of regular and irregular shape, Powder Technol. **182**, 342 (2008).

[30] D. De Souza, T. Zürner, and R. Monchaux, Simple distinction of similar-looking inertial particles and fluid tracers on camera images, Exp. Fluids **62**, 114 (2021).

[31] B. Wieneke, Stereo-PIV using self-calibration on particle images, Exp. Fluids **39**, 267 (2005).

[32] J. C. Crocker, D. G. Grier, and E. R. Weeks, Particle tracking using IDL, http://www.physics.emory.edu/faculty/weeks/idl/ (1999).

[33] D. Blair and E. Dufresne, Matlab Particle Tracking, http://site.physics.georgetown.edu/matlab/index.html (2007).

[34] W. K. George and H. J. Hussein, Locally axisymmetric turbulence, J. Fluid Mech. **233**, 1 (1991).

[35] M. Piirto, H. A. T. Ihalainen, H. Eloranta, and P. Saarenrinne, 2D spectral and turbulence length scale estimation with PIV, J. Visualization **4**, 39 (2001).

[36] P. Saarenrinne, M. Piirto, and H. Eloranta, Experiences of turbulence measurement with PIV, Meas. Sci. Technol. **12**, 1904 (2001).

[37] S. Baldi and M. Yianneskis, On the Direct Measurement of Turbulence Energy Dissipation in Stirred Vessels with PIV, Ind. Eng. Chem. Res. **42**, 7006 (2003).

[38] A. Aliseda, A. H. Cartellier, F. Hainaux, and J. C. Lasheras, Effect of preferential concentration on the settling velocity of heavy particles in homogeneous isotropic turbulence, J. Fluid Mech. **468**, 77 (2002).

[39] R. Monchaux and A. Dejoan, Settling velocity and preferential concentration of heavy particles under two-way coupling effects in homogeneous turbulence, Phys. Rev. Fluids **2**, 104302 (2017).

[40] R. Monchaux, M. Bourgoin, and A. Cartellier, Preferential concentration of heavy particles: A Voronoï analysis, Phys. Fluids **22**, 103304 (2010).

[41] R. Monchaux, M. Bourgoin, and A. Cartellier, Analyzing preferential concentration and clustering of inertial particles in turbulence, Int. J. Multiphase Flow **40**, 1 (2012).

[42] H. Wang and A. Wing-Keung Law, Second-order integral model for a round turbulent buoyant jet, J. Fluid Mech. **459**, 397 (2002).

[43] R. N. Parthasarathy and G. M. Faeth, Turbulent dispersion of particles in self-generated homogeneous turbulence, J. Fluid Mech. **220**, 515 (1990).

[44] C. C. K. Lai and S. A. Socolofsky, The turbulent kinetic energy budget in a bubble plume, J. Fluid Mech. **865**, 993 (2019).